Accelerated constant current stress on triple cation perovskite solar cells

Nicolò Lago [a],[*], Sathy Harshavardhan Reddy [b], Erica Magliano [b], Aldo Di Carlo [b], Andrea Cester [a]

[a] *Department of Information Engineering, University of Padova, 35131, Padova, Italy*
[b] *Department of Electronic Engineering, University of Rome "Tor Vergata", 00133, Roma, Italy*

ARTICLE INFO

ABSTRACT

The increasing demand for renewable and cost-effective energy sources requires not only the development of alternative solar technologies, but these new technologies must be stable enough to be used in a real-life application. For this reason, perovskite solar cells (PSCs) must be investigated not only in terms of power conversion efficiency, but also in terms of reliability. In this work, accelerated forward current stress is applied as a tool to investigate PSCs stability and degradation kinetic emulating real-life scenarios. The choice of the hole-blocking layer (HBL) plays a crucial role in PSCs intrinsic instability as well as in their degradation rate, which follows a stretched exponential law. Here, tin oxide (SnO_X) and bathocuproine (BCP) are investigated as HBLs observing that for low stress currents BCP-based PSCs degrade faster than SnO_X-based PSCs, whereas for large stress currents SnO_X-based PSCs degrade faster than BCP-based PSCs. The results also indicated that the major cause of degradation in the devices is primarily driven by the formation of shunt paths leading to cell breakdown. Our findings offer valuable insights for improving the stability of PSCs under accelerated stress conditions and provide useful information for the design of PSC-based solar panels depending on their field of applications.

1. Introduction

Among the emerging photovoltaic technologies, perovskite solar cells (PSCs) are surely one of the most promising because they quickly achieved a certified power conversion efficiency of 25.7%, which is close to the 26.7% of crystalline silicon [1]. The reason behind this outstanding performance relies on the perovskite large absorption coefficient [2] (notably, Si/Perovskite tandem cells with efficiencies up to 31.3% are being exploited [1]) and its remarkable high defect tolerance [3], which allows the processing of highly performing solar cells in spite of the use of low-cost techniques.

Despite the high-power conversion efficiencies, both short-term and long-term stability of perovskite-based solar cells is still a crucial limiting factor. In such a contest, most studies focus on the role of ion and ion vacancies displacement to explain current-voltage hysteresis [4, 5], or on the long effects of interfacial ions accumulation that leads to open-circuit voltage instabilities [6] as well as to the degradation of the charge extraction layers [7]. The latter is particularly worthy of investigation, in fact, to understand whether the PSC technology is ready to enter the market of energy production (either large-scale solar panels or single cells for low power devices), it is mandatory to investigate the

degradation of the cells during their nominal operative conditions. This is achieved by performing accelerated stresses that allow finding the degradation mechanisms of solar cells when subjected to a specific stress condition like thermal [8,9], electrical [10,11], mechanical [12,13], environmental [14,15], or a combination of the above [16,17].

Although most of the literature reports the stability of PSCs under shelf-life [18,19], light illumination [20,21], and temperature conditions [22,23], there is limited emphasis on evaluating stress under electrical bias [24]. In particular, there are almost no articles reported specifically on the constant-current stress for PSCs [25]. Such an aspect is of particular importance because it allows to test cells in a realistic stressful environment like a partially shaded solar panel in which cells can be subjected to very large forward currents.

In this work, we performed accelerated forward current stresses on two PSC architectures differing each other for the choice of the hole-blocking layer (HBL), either tin oxide (SnO_X) or bathocuproine (BCP). We observed that devices degradation and failure is primarily driven by the formation of shunt paths that lead to the cell breakdown. Our analysis shows that the choice between BCP and SnO_X has a large impact not only on stress-induced degradation, but also on the intrinsic stability of the PSC, with BCP being far more stable than SnO_X. Therefore, we

* Corresponding author.
E-mail address: lagonico@dei.unipd.it (N. Lago).

modeled both the degradation kinetic and intrinsic instability of the two architectures, and we found out that the BCP cell are more robust for large stress condition whereas the SnO_X-based cells are more suited for low stress conditions, which is an important information for the design and fabrication of PSC solar modules.

2. Materials and methods

2.1. Materials

Poly[bis(4-phenyl)(2,4,6-trimethylphenyl)amine] (PTAA) (Solaris Chem) [6,6],-phenyl-C61-butyric acid methyl ester (PCBM-99%-Solenne), bathocuproine (BCP-96%-Sigma-Aldrich), SnO_X ink (N31-Avantama), methylammonium bromide (MABr-99.99%-Greatcell solar), (FAI-99.99%-Greatcell solar), cesium iodide (CsI-99.99%-Sigma-Aldrich), lead bromide (PbBr2-TCI), lead iodide (PbI2-TCI), 1-butyl-3-methylimidazolium tetrafluoroborate (BMITFB-98%-ACROS), Dimethylformamide (DMF-anhydrous-Sigma-Aldrich), dimethyl sulfide (DMSO-anhydrous-Sigma-Aldrich), toluene (anhydrous-Sigma-Aldrich), chlorobenzene (CB-anhydrous-Sigma-Aldrich), dichlorobenzene (DCB-anhydrous-Sigma-Aldrich).

2.2. Device fabrication

Fig. 1 reports the architecture of the cells used in this work. Both types of cells are based on a triple cation (3C) perovskite with BMIM-BF$_4$ as ionic liquid additive (IL) sandwiched between PTAA (hole-transport material) and PCBM (electron-transport material) in an inverted configuration. The two architectures differ only in the HBL, which is SnO_X and BCP, respectively.

Cells were fabricated starting from patterned ITO/glass substrates. The substrates were cleaned in an ultrasonic bath with a detergent solution (2% Hellmanex in deionized water), followed by deionized water, acetone, and 2-propanol, each for 15 min. After drying, they were treated for 15 min in a UV/O$_3$ tool (Novasonic). PTAA in toluene (2 mg/mL) was spun at 5000 rpm for 30 s before being annealed at 100 °C for 10 min. After cooling, the samples were exposed to UV light for 5 min to improve the surface wettability of the PTAA. The perovskite precursor with molecular formula $Cs_{0.05}MA_{0.14}FA_{0.81}PbI_{2.7}Br_{0.3}$ (1.4 M) in DMF: DMSO 3.16:1 was spin-coated at 4000 rpm for 35 s before dropping 180 μl of CB after 20 s [26,27]. Then, the film was annealed for 10 min at 100 °C. Lastly, PCBM was spun at 1700 rpm for 30 s and subsequently annealed at 100 °C for 5 min.

For the SnO_X architecture, SnO_X ink (N31-Avantama) was filtered with a 0.45 μm PVDF filter and then spun at 5000 rpm for 35 s before annealing at 120 °C for 20 min. Then, before copper deposition, ITO was sputtered on top of the SnO_X layer to prevent Cu electromigration [27]. For the BCP-based architecture, BCP in isopropanol (0.5 mg/ml) was spun at 4000 rpm for 30 s.

Finally, 100 nm of Cu was evaporated defining the cell active area of 0.24 cm^2 for the SnO_X architecture and 0.18 cm^2 for the BCP architecture.

2.3. Stress and characterization procedure

Cells were characterized by standard current vs. voltage (I–V) characteristics performed both in dark and under illumination. The voltage was scanned from 0 V up to 1.2 V with a scan rate of 200 mV/s. For cell illumination we used a high-power chip-on-board white LED array with an emitting area of 4 cm^2 to guarantee a stable and uniform light spot and a fine-tuning of the light intensity for prolonged times. In order to account for the spectral mismatch between the LED spectrum and the reference spectrum AM1.5G, the LED intensity was calibrated at 1 sun for each sample by means of external-quantum-efficiency (EQE) measurements, in agreement with the International Electrochemical Commission standard IEC 60904-7-2019 [28].

Constant Current Stresses (CCSs) were performed in dark by forcing a forward current bias through the cells. This stress condition is equivalent to a partially shaded solar panel in which the current photogenerated by the illuminated cells partially flows into the shaded cells [29]. Depending on the working conditions of the solar panel (light intensity, external load, and the number of cells shaded and illuminated) the intensity of the forward current flowing through the shadowed cells may largely vary. For this reason, we performed CCS for different values of stress currents (J_{STRESS}) ranging from 200 mA/cm^2 up to 800 mA/cm^2. In addition, to monitor the intrinsic behavior of the cells during the same time span of the stress, we also repeated the same stress procedure forcing $J_{STRESS} = 0$ A/cm^2 (later in the text, we will refer to this stress as reference-CCS). As depicted in Fig. 2, stresses were periodically interrupted to monitor the state of the cells by performing I–V characterizations of the cells under test.

2.4. SEM cross-sectional images and EDX elemental maps

The scanning electron microscopy (SEM) cross-sectional images were acquired by using field emission SEM (FESEM, Tescan Mira 3 LMU FEG). The energy-dispersive X-ray spectroscopy (EDX) elemental maps were performed with the Xplore detector by Oxford Instruments.

3. Discussion

Before stress, cells performance was characterized by their EQE spectra and by performing current-vs-voltage measurements in dark and light conditions.

Fig. 3 shows the typical EQE of the two cell architectures under investigation. The two architectures display similar EQEs with a quasi-uniform response in the range between 400 nm and 750 nm (above
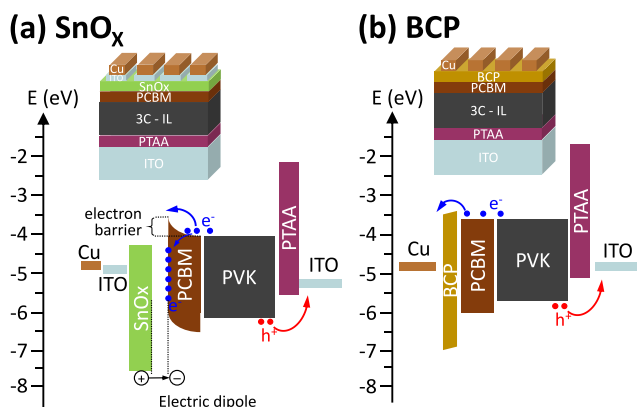

Fig. 1. Layout and qualitative flat-band diagram of the cells used in this work. (a) Is the SnO_X-based cells; (b) is the BCB-based cells.
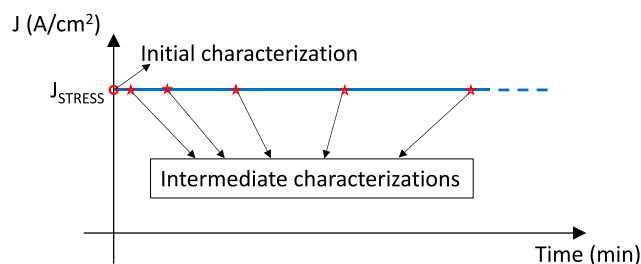

Fig. 2. Example of Constant Current Stress Procedure. The monitoring of the cell performance is done in a logarithmic fashion.
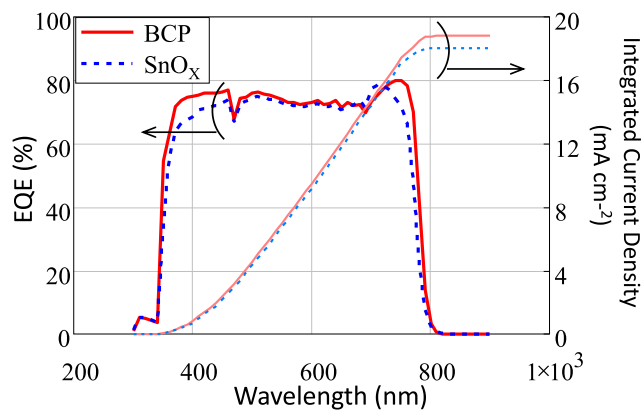
Fig. 3. External Quantum Efficiency spectra of the two architectures (left axis). The red-solid line is the BCP-based cell; the blue-dashed line is the SnO$_X$-based cell. The right axis reports the corresponding integrated current density.

70% EQE efficiency). This is expected because both architectures share the same active layers and differ only in the hole-blocking layer. From EQE measurements it is possible to compute the short circuit current J$_{SC}$ with respect to the AM1.5G spectrum. Given the similar EQE spectra, the two architectures also feature similar J$_{SC}$ around 17 mA/cm^2, with the SnO$_X$-based cells featuring a short-circuit current slightly larger than the BCP-based ones.

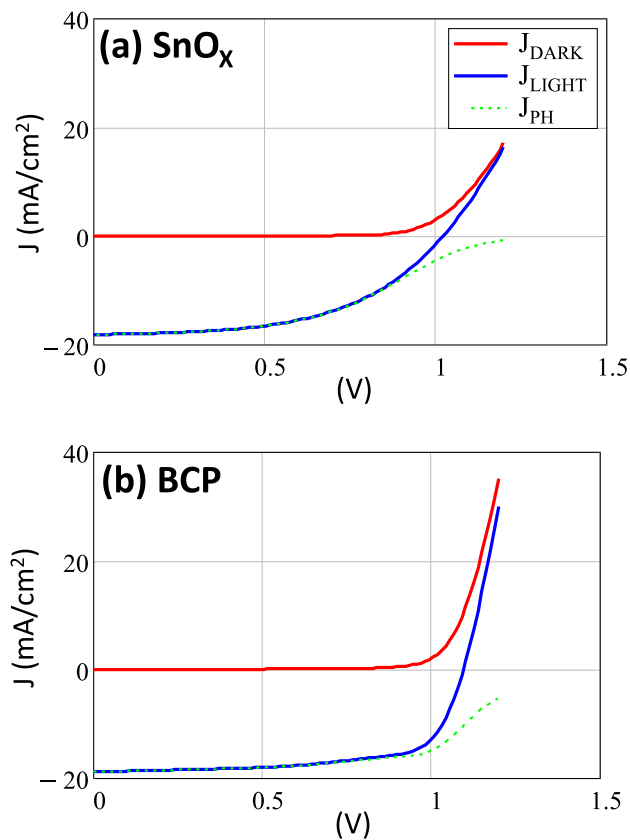Fig. 4 shows the typical I–V characteristics of the two architectures

Fig. 4. Current vs Voltage characteristics representative of the two architectures, (a) SnO$_X$, (b) BCP. Red-solid curves are the current measured in dark (J$_{DARK}$), blue-solid curves are the currents measured under 1 sun illumination (J$_{LIGHT}$), green-dashed curves are the cell photocurrent (J$_{PH}$).

recorded before the stress. Although the BCP-based cells display larger currents in dark (J$_{DARK}$), they feature improved light-conversion capabilities, as shown by the larger efficiency obtained from the currents measured in light condition (J$_{LIGHT}$): η ≈ 10%, compared to 9% of the SnO$_X$-based cells. Compared to state-of-the-art solar cells [1], our devices are characterized by a relatively low power conversion efficiency that is most likely due to sputtering-induced damages of the SnO$_X$ layer, as demonstrated in our previous work showing that a 20% efficiency is possible by optimizing the perovskite ink and the sputtering parameters [27]. However, since our work focuses on device reliability rather than efficiency, to get a clear picture of the degradation dynamics we decided to carry on our investigation with devices characterized by a lower efficiency but featuring a larger long-term stability.

For a deeper investigation, Fig. 4 reports also the cells photocurrent density J$_{PH}$ (green-dashed lines) computed as J$_{PH}$ = J$_{LIGHT}$ − J$_{DARK}$. The validity of this equation is justified by the fact that the two architectures exhibit a very small in-series resistance that we estimated to be less than 4 Ω cm^2 for both architectures, therefore the voltage drop across it is negligible.

The comparison of the two photocurrents allows us to understand the efficiency difference between the two architectures. In fact, for the SnO$_X$-based cells, J$_{PH}$ follows a modified Sokel-Hughes model [30] (opportunely modified to account for the presence of a selective contact); whereas, for the BCP-architecture J$_{PH}$ is roughly constant up to 1 V, highlighting a quasi-ideal behavior. This difference directly reflects on the cells' parameters, with the BCP-architecture being characterized by a larger open-circuit voltage (V$_{OC}$ ≈ 1.1 V with BCP; V$_{OC}$ ≈ 1 V with SnO$_X$) and noticeably larger Fill-Factor (FF ≈ 70% with BCP; FF ≈ 50% with SnO $_X$). The origin of the difference between the two photocurrents can be explained using the band diagrams reported in Fig. 1. In fact, as explained in Ref. [31], interfacial recombination at SnO$_X$/PCBM interface induces the formation of an electric dipole that reduces the built-in voltage and create an energy barrier that limits the extraction of electrons. However, the introduction of BCP as hole-blocking-layer, prevents charge accumulation at the PCBM interface [32], thus promoting a more efficient extraction of electrons and resulting in an ideal photocurrent behavior.

To investigate the reliability of the cells, we performed CCS on both architectures. Fig. 5 reports the efficiency of the cells monitored during CCS for different values of J$_{STRESS}$, whereas Fig. 6 shows the I–V -light characteristics during CCS for J$_{STRESS}$ = 800 mA/cm^2. To monitor the intrinsic stability of our samples, Fig. 5 reports also the results obtained during reference-CCS. The BCP architecture appears as stable for the entire stress timescale, with just a marginal increase of efficiency during time; on the other hand, the SnO$_X$ architecture displays a very large instability right from the beginning. This reflects in an initial increase in efficiency (around 50% larger) followed by a slow degradation.

The accelerated stresses at increasing J$_{STRESS}$ (from 200 mA/cm^2 to 800 mA/cm^2) initially follow the same intrinsic behavior visible during the reference-CCS (J$_{STRESS}$ = 0 A/cm^2). This is especially evident in the SnO$_X$ architecture for J$_{STRESS}$ = 200 mA/cm^2 (low-stress condition). In this case, the efficiency evolution closely follows that of reference-CCS until roughly 200 min. Increasing J$_{STRESS}$, the degradation kinetic changes after some tens of seconds. This experimental evidence indicates that the devices can withstand high current densities (10–80 times larger than J$_{SC}$) only for short time periods. After this initial phase, the applied forward current begins to degrade the cells under test, and the recorded efficiency decreases irreversibly. Fig. 5 clearly shows this accelerated behavior: the larger J$_{STRESS}$, the faster the efficiency droop.

Similar degradation trends with the increase of electrical stress was reported by Bae et al. for MAPbI$_3$-based cells featuring similar V$_{OC}$ around 1 V [24]. In their work, they performed forward voltage stresses showing that applying a constant voltage V$_{STRESS}$ = 1.2 V cell breakdown is reached in just a few hours. Monitoring V$_{STRESS}$ during CCS, we observe that the voltage drop during stress goes from around 1.6 V (200 mA/cm^2) to 2.7 V (800 mA/cm^2) for BCP cells, whereas it goes from 2 V
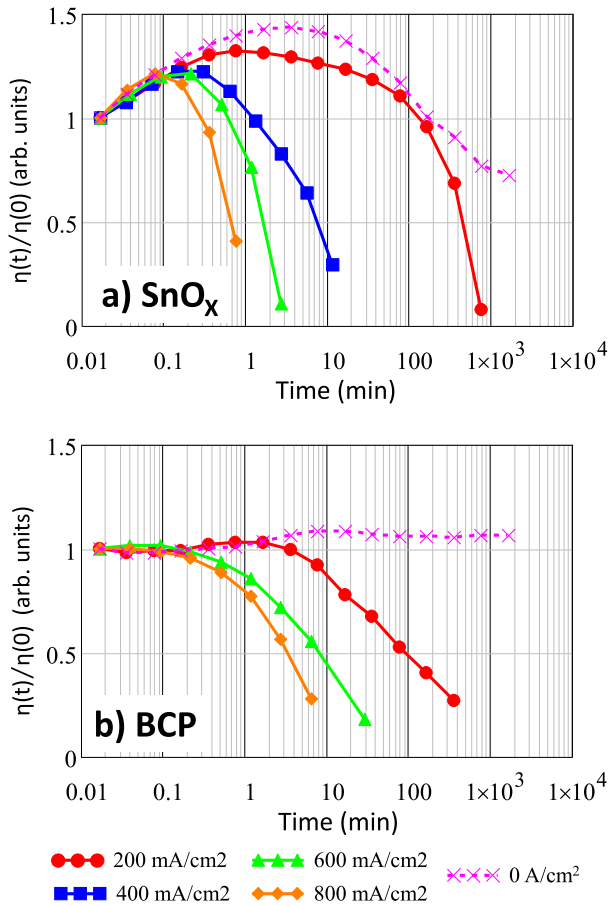
Fig. 5. Cells' efficiency monitored during CCS at different J_{STRESS} values. Panel (a) reports the efficiency for the SnO_X architecture, whereas panel (b) reports the efficiency for the BCP architecture.

Fig. 6. Representative I–V-light characterizations during CCS for $J_{STRESS} = 800$ mA/cm^2. Panel (a) is the SnO_X architecture, whereas panel (b) is the BCP architecture. Blue-solid lines are the I–V characteristics before stress, whereas red-solid lines are the I–V curves before breakdown. Arrows indicated the increasing stress-steps.

Fig. 7. Time required to lose 50% of the initial efficiency.

up to 4 V for SnO_X cells, confirming the higher reliability of our cells with respect to previous reports.

For a quick comparison of the two architectures, we arbitrarily defined the threshold time T_{50} as the time at which a 50% efficiency droop is recorded (Fig. 6). For large J_{STRESS} values, the BCP architecture appears more robust since its efficiency drop stays below 50% for longer times than the SnO_X architecture. However, for lower J_{STRESS} values, the SnO_X architecture has a lower degradation rate than the BCP architecture.

As highlighted in Fig. 7, the two architectures display two different degradation acceleration as a function of J_{STRESS}: for J_{STRESS} larger than 350 mA/cm^2 (around 20 times J_{SC}) the BCP architecture is more robust, whereas for J_{SRESS} smaller than 350 mA/cm^2 the SnO_X architecture is more reliable. This difference must be considered in the design of a solar panel where in-series stripes of cells are connected in parallel to increase the panel output power. In fact, as depicted in Fig. 8, a forward current is forced through a cell when some of the stripes are shadowed while other stripes are illuminated. In the worst-case scenario, the current flowing through a shadowed cell is J_{SC}·(N-1), with N being the number of stripes composing the solar module. Therefore, using the SnO_X architecture, a panel should contain less than 20 cells connected in parallel, thus ensuring a low forward current in case of a partially shadowed panel; otherwise, if higher output currents are required, and more than 20 cells in parallel are needed, the BCP architecture should be preferred since it can withstand larger forward currents.

To better understand the efficiency droop during CCS, we also extrapolated the principal figures of merit that are reported in Fig. 9
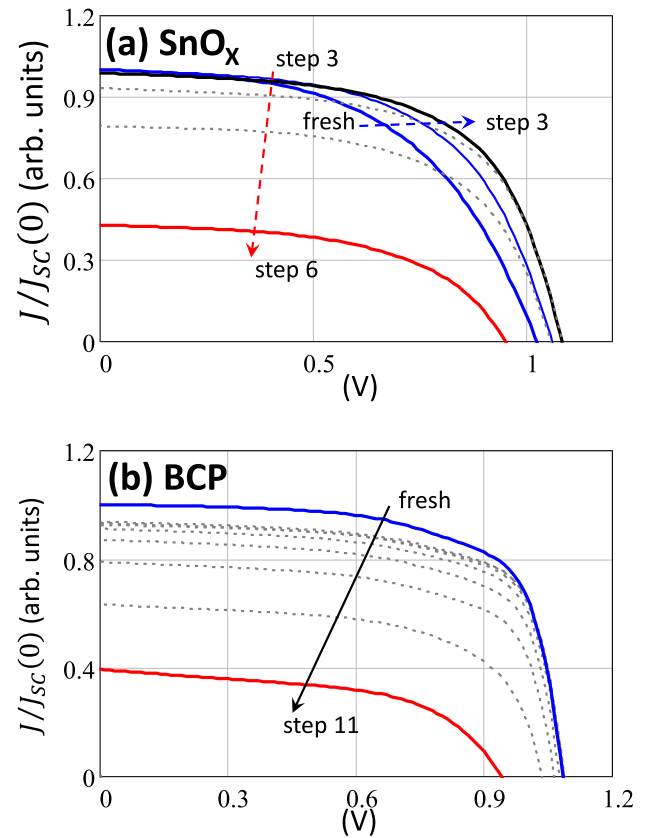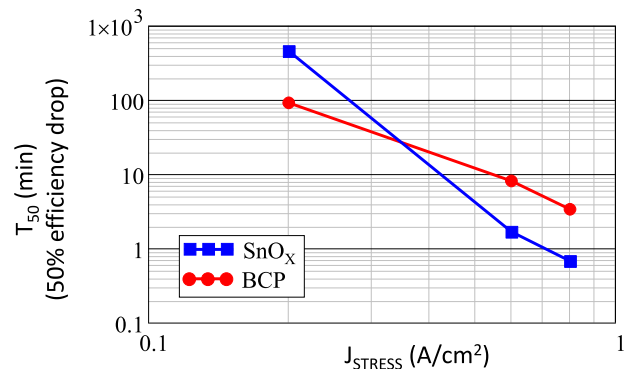
(namely, V_{OC}, J_{SC}, and FF). From the behavior of these parameters during stress, we observe that the main effect of CCS is to induce a strong degradation of J_{SC}, followed by the worsening of FF. These evidences suggest that cells degradation during CCS occurs following two phases.

- An initial phase in which part of the stress current flows through pre-existing shunts and weak spots (e.g., where there is a higher electric field), causing a local high-power dissipation able to irreversibly damage the perovskite layer, thus reducing the active area of the
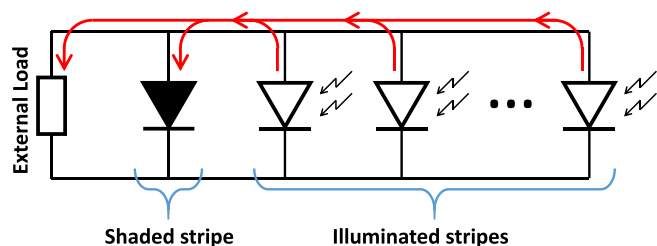
Fig. 8. Example of a partially shaded solar module illustrating the flow of current through the circuit. Each branch can represent either a single cell or multiple cells connected in series.

cells with a consequent decrease in the J_{SC} current, clearly visible also from the I–V characteristics in Fig. 6.

- When the current is applied for a prolonged time, new shunts are created, contributing to the decrease in both J_{SC} and FF until the complete breakdown of the cell, which is anticipated by an important negative shift of V_{OC} (see Fig. 6).

Our reasoning is further corroborated by the SEM cross-sectional images acquired before and after CCS and reported in Fig. 10. In particular, comparing fresh and degraded SnO_X-based cells (Fig. 10a and b and c, respectively) we can detect, not only the electromigration of the ITO/Cu cathode electrode towards the anode electrode (Fig. 10c), but also the degradation of the PTAA layer contributing to the pinholes formation and leading to a partial detachment of the perovskite layer electrode (as highlighted in Fig. 10b). This PTAA degradation is present also in the BCP-based architecture where it is easier to observe also the
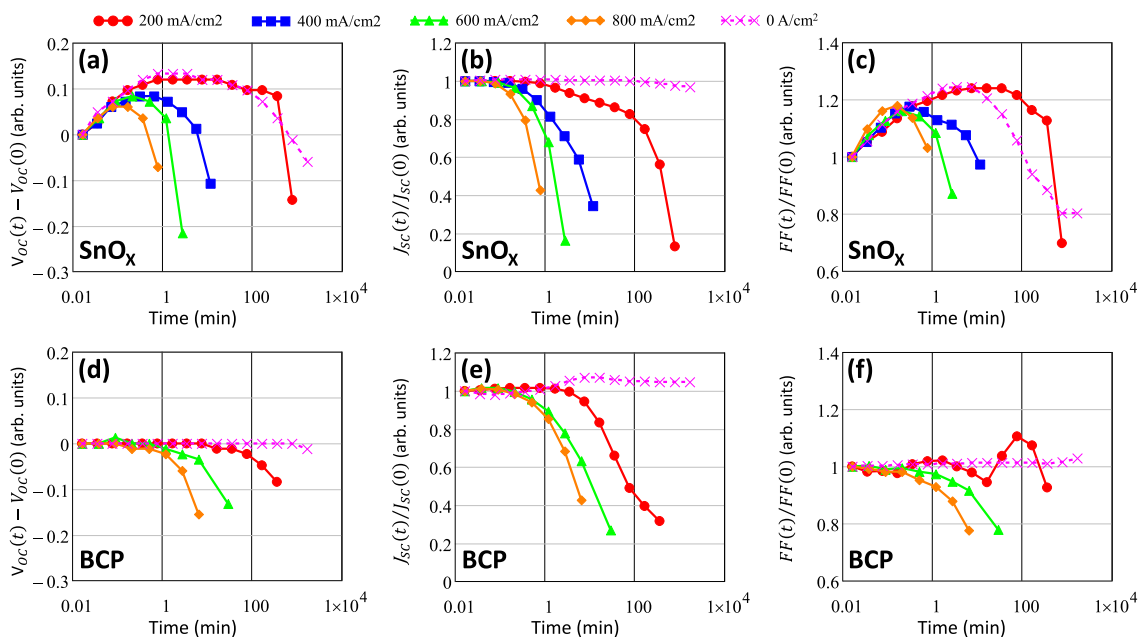

Fig. 9. Figures of merit (V_{OC}, J_{SC}, and FF) of the cells during CCS. (a), (b) and (c) are the SnO_X-based cells V_{OC}, J_{SC}, and FF, respectively; (d), (e) and (f) are the BCP-based cells V_{OC}, J_{SC}, and FF, respectively.
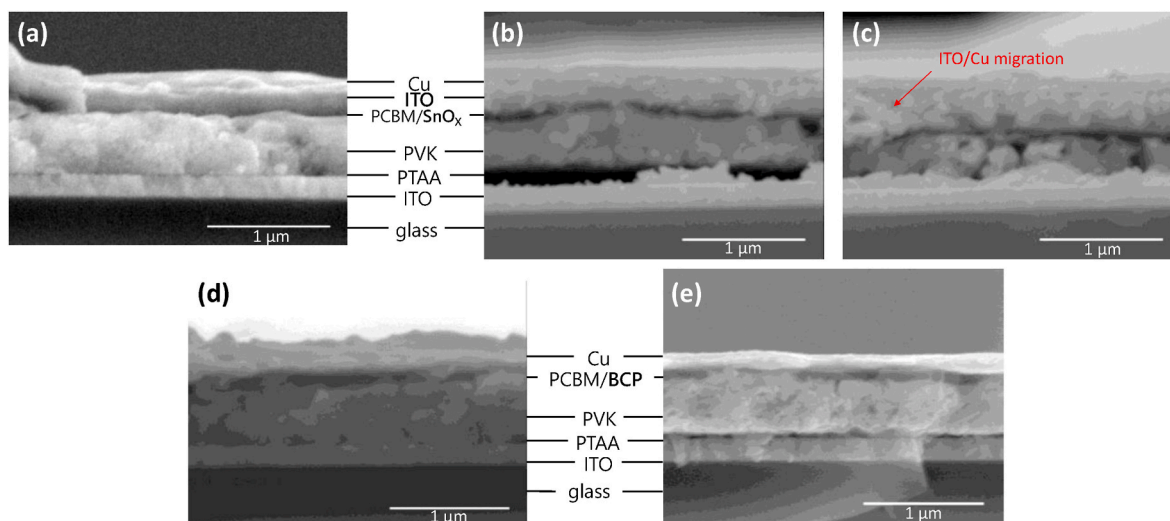

Fig. 10. Cross-sectional SEM images of the SnO_X-based devices before (a) and after (b, c) CCS and of the BCP-based devices before (d) and after (e) CCS.

degradation of the perovskite layer that undergoes a change of phase from a typical poly-crystalline structure (Fig. 10d) towards a more amorphous morphology (Fig. 10e), which is likely influenced by ions migration during stress [33]. In addition, Cu electromigration into the perovskite layer can induce the formation of clusters further changing the morphology of the perovskite layer.

A clearer picture of cells' degradation is obtained by analyzing the EDX elemental maps reported in Fig. 11. At this purpose, we targeted five elements, namely, Pb, I, In, Cu, and Sn. The Pb and I maps give us a clear picture of the perovskite layer before and after the stress. Before the stress, both Pb and I are well-confined between the PTAA and PCBM layers, whereas, after CCS, the two metals show a wider distribution indicating the degradation of all the three layers (PTAA, perovskite, and PCBM). Instead, the In, Cu, and Sn maps allow to identify the anode and cathode electrodes. In particular, In and Sn are present inside the ITO and SnO_X layers, therefore are initially located on both anode and cathode in the SnO_X-based cells, whereas they are present only at the anode electrode in the BCP-based cells. For both the SnO_X and BCP-based architectures, the anode electrode composition (ITO) is not affected by CCS as its metal composition remain unchanged after the stress. Conversely, the cathode undergoes a strong electromigration towards the anode. Specifically, the Cu atoms are able to cross the entire stack of the cells reaching the ITO anode contact confirming that the

major cause of cells degradation during CCS is the formation of new shunt paths during stress. Notably, the Cu maps in Fig. 11 show also that Cu electromigration is facilitated in SnO_X-based cells with respect to BCP-based cells, explaining the larger instability of SnO_X-based cells during high-current CCS. In the case of the $SnOx$-based devices, In and Sn migration is observed as well, which further induce the formation of pinholes.

Since J_{SC} is the main parameter responsible for the efficiency degradation during stress, we decided to model its behavior starting from the degradation kinetics described by J.W. McPherson [34]. Among the three main degradation models reported in Ref. [34] (exponential, logarithmic, and power law), we see that the two architectures are best described by a stretched exponential degradation law:

$$S(t) = \exp\left\{ - [A_0(t - t_0)]^\beta \right\}, \qquad (1)$$

where A_0 is the degradation rate with unit s^{-1}, and t_0 is the time delay before the start of the degradation during stress that we found to be $t_0 = 0$ s, indicating that cells degradation begins as soon as the stress is applied. Similar decaying models have already been used for interpreting the degradation kinetics of PSC subjected to light stresses [35, 36], confirming the choice of an exponential law to fit our data (instead of the logarithmic and power laws). The stretched exponential factor β is
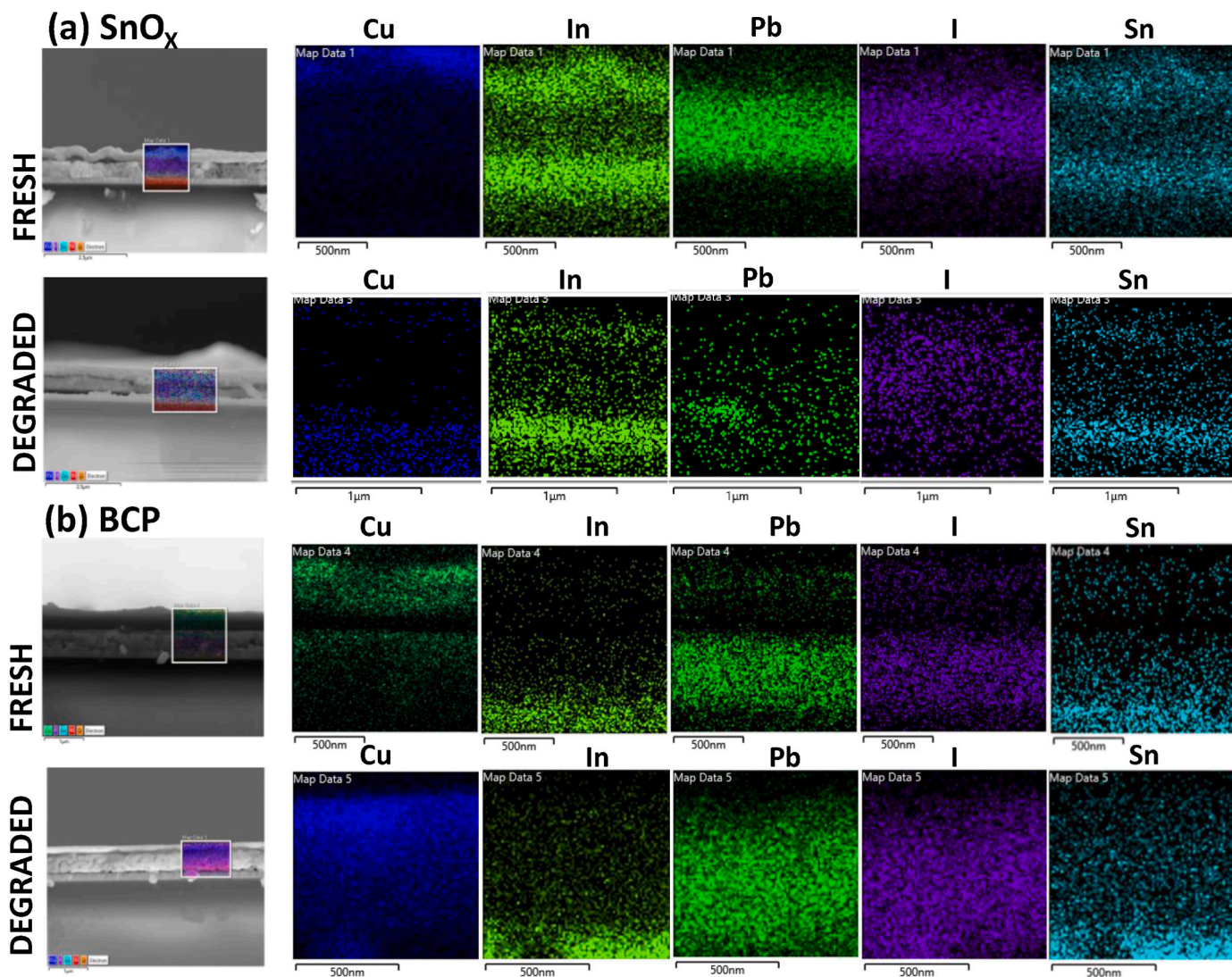

Fig. 11. –Cross-sectional SEM images (on the left) and EDX elemental maps (on the right) of fresh and degraded SnO_X – (a) and BCP-based (b) devices. The EDX maps show the elemental distribution of Cu, In, Pb, I, Sn of the area selected in the respective SEM image on the left.

introduced to consider the possible presence of different degradation mechanisms with similar time constants.

Even though equation (1) is suitable to describe degradation parameters of most devices, as discussed above, the solar cells under investigation are characterized by an intrinsic instability clearly visible during reference-CCS. For this reason, to properly describe J_{SC} behavior during stresses, our model needs to take into account for the intrinsic instability of the cells. This is done by introducing two decaying exponentials, one to describe the initial increase of performance visible in both BCP and SnO$_X$ architectures and one to account for the slow intrinsic degradation observed in the SnO$_X$ architecture [37]. Thus, J_{SC} during reference-CCS is modeled as follows:

$$Z(t) = B_{I1}[1 - \exp(-C_{I1}(t - t_{I1}))] \bullet H(t - t_{I1}) - B_{I2}[1 - \exp(-C_{I2}(t - t_{I2}))]$$
$$\bullet H(t - t_{I2}), \tag{2}$$

where B_{Ii} (i = 1,2) is the magnitude of the intrinsic instability, C_{Ii} is the exponential decay rate describing how fast the intrinsic instability is occurring, and t_{Ii} is the time delay with respect to the beginning of the stress. $H(t)$, instead, is the step function defined as:

$$H(x) = \begin{cases} 0, & t < 0 \\ 1, & t \geq 0 \end{cases} \tag{3}$$

Therefore, combining (1) and (2), we can model the short-circuit current during stress as:
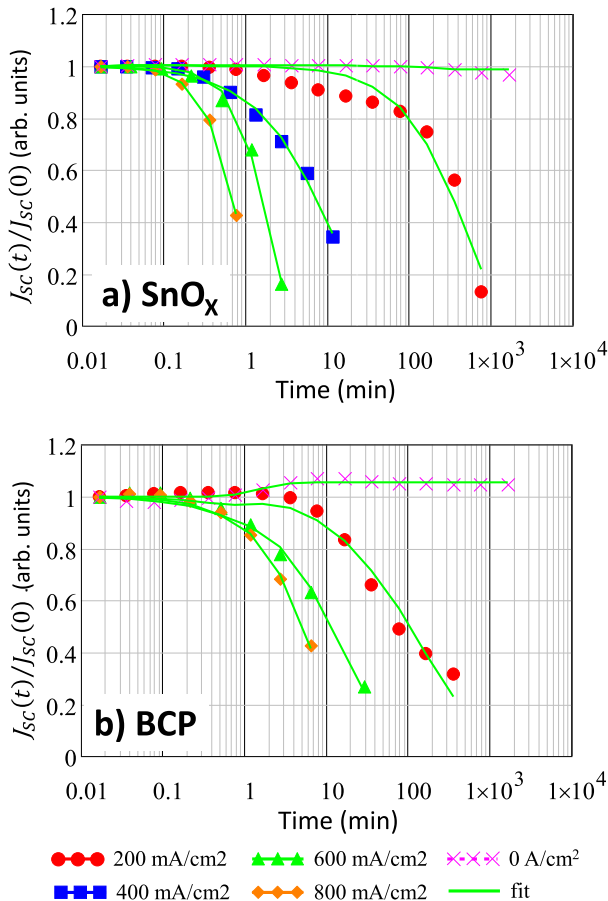
$$\frac{J_{sc}(t)}{J_{SC}(0)} = S(t) + Z(t) \tag{4}$$

The goodness of the model is reported in Fig. 12, which shows the fitting of J_{SC} for different stress currents, whereas Fig. 13 shows the evolution of the degradation parameters as a function of the stress current.

Regarding the reference-CCS, in our previous study [37] we showed that the BCP architecture is intrinsically more stable than the SnO$_X$ architecture (see efficiency plot Fig. 5); however, focusing on the short circuit current, we observe that the BCP architecture is slightly more unstable presenting a 5% current increase with respect to the beginning of the stress (highlighting the importance of analyzing CCSs and reference-CCS separately). Conversely, the SnO$_X$ architectures feature only a 1.5% oscillation due to a small degradation of the cells that are likely due to the presence of dispersing agents in the commercial SnO$_X$ ink [27].

Similarly to the reference-CCS, equation (4) confirms that the two architectures degrade with two different decaying rates. Fig. 12 shows the degradation rate A_0 as a function of J_{STRESS}. As expected, A_0 monotonically increases with the increase of J_{STRESS} (accelerated stress). Remarkably, for low current stresses the BCP architecture degrades faster than the SnO$_X$ architecture; however, for larger J_{STRESS} the SnO$_X$ architecture is the one with the faster degradation.

This analysis is in direct agreement with the interpretation of the threshold time T_{50} (Fig. 7) confirming that the main effect of CCS is the reduction of the short-circuit current with the continuous formation of new shunts that reduces the devices active area.

4. Conclusion

In this work, we performed accelerated forward current stresses on triple cation inverted PSCs. As a case study, we fabricated cells differing only on the choice of the HBL, namely, SnO$_X$ and BCP. The two architectures are characterized by similar performances (EQE, and J_{SC}), therefore they are the perfect candidates for a comparison.

To investigate cells degradation, we performed CCS for increasing J_{STRESS} and we modeled distinctly the intrinsic instability of the cells and the CCS-induced degradation that follows an exponential law for both architectures. Furthermore, forward CCS mainly affects the short-circuit current and the fill-factor, suggesting that the major cause of degradation is the formation of shunt paths that lead to the cell breakdown.

Comparing the two architectures (SnO$_X$ and BCP), we observed that they feature different degradation rates. In particular, for large stress currents (roughly $J_{STRESS} > 20 \cdot J_{SC}$) the SnO$_X$-based cells degrade faster than the BCP-based cells, whereas, for small stress currents ($J_{STRESS} < 20 \cdot J_{SC}$) the BCP-based cells degrade faster than the SnO$_X$-based cells. This is an important result for the design of PSC modules by taking into
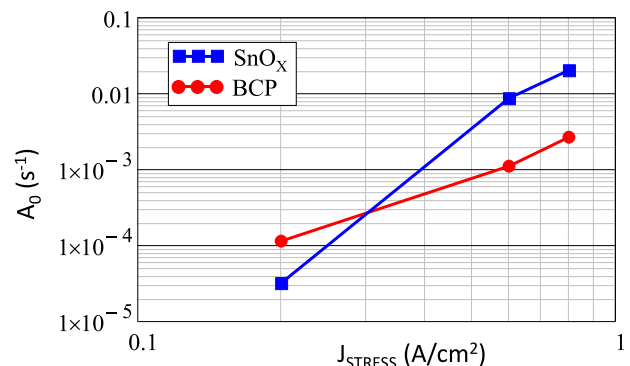

Fig. 12. Fitting of the short-circuit current J_{SC} with the proposed model for both (a) the SnO$_X$ architecture, and (b) the BCP architecture.

Fig. 13. Degradation coefficient A_0 as a function of stress current J_{STRESS}.

account the maximum forward current that a single cell can sustain in the possible event of partial shading of the solar panel, with the BPC architecture being more indicated to withstand large forward currents (i.e. more than 20 cells in parallel), while the SnO_X are more indicated for low current stresses (less than 20 cells in parallel).

Funding information

CRediT authorship contribution statement

Nicolò Lago: Writing – review & editing, Writing – original draft, Software, Investigation, Formal analysis, Data curation, Conceptualization. **Sathy Harshavardhan Reddy:** Writing – review & editing, Investigation. **Erica Magliano:** Data curation. **Aldo Di Carlo:** Resources, Project administration, Funding acquisition. **Andrea Cester:** Writing – review & editing, Supervision, Project administration, Funding acquisition.

Declaration of competing interest

The authors declare that they have no known competing financial interests or personal relationships that could have appeared to influence the work reported in this paper.

Data availability

Data will be made available on request.

Acknowledgments

References

[1] Best Research-Cell Efficiency Chart | Photovoltaic Research | NREL, Available online. https://www.nrel.gov/pv/cell-efficiency.html (accessed on March 30, 2023).

[2] S. De Wolf, J. Holovsky, S.-J. Moon, P. Löper, B. Niesen, M. Ledinsky, F.-J. Haug, J.-H. Yum, C. Ballif, Organometallic halide perovskites: sharp optical absorption edge and its relation to photovoltaic performance, J. Phys. Chem. Lett. 5 (2014) 1035–1039, https://doi.org/10.1021/jz500279b.

[3] J. Kang, L.W. Wang, High defect tolerance in lead halide perovskite CsPbBr3, J. Phys. Chem. Lett. 8 (2017) 489–493, https://doi.org/10.1021/acs.jpclett.6b02800.

[4] C. Li, A. Guerrero, S. Huettner, J. Bisquert, Unravelling the role of vacancies in lead halide perovskite through electrical switching of photoluminescence, Nat. Commun. 91 (9) (2018) 1–8, https://doi.org/10.1038/s41467-018-07571-6, 2018.

[5] D.H. Kang, N.G. Park, On the current–voltage hysteresis in perovskite solar cells: dependence on perovskite composition and methods to remove hysteresis, Adv. Mater. 31 (2019) 1805214, https://doi.org/10.1002/adma.201805214.

[6] F. Ebadi, M. Aryanpour, R. Mohammadpour, N. Taghavinia, Coupled ionic-electronic equivalent circuit to describe asymmetric rise and decay of photovoltage profile in perovskite solar cells, Sci. Rep. 91 (9) (2019) 1–9, https://doi.org/10.1038/s41598-019-48505-6, 2019.

[7] A. Rizzo, F. Lamberti, M. Buonomo, N. Wrachien, L. Torto, N. Lago, S. Sansoni, R. Pilot, M. Prato, N. Michieli, M. Meneghetti, G. Meneghesso, A. Cester, Understanding lead iodide perovskite hysteresis and degradation causes by extensive electrical characterization, Sol. Energy Mater. Sol. Cells 189 (2019) 43–52, https://doi.org/10.1016/j.solmat.2018.09.021.

[8] D.B. Khadka, Y. Shirai, M. Yanagida, K. Miyano, Insights into accelerated degradation of perovskite solar cells under continuous illumination driven by thermal stress and interfacial junction, ACS Appl. Energy Mater. 4 (2021) 11121–11132, https://doi.org/10.1021/acsaem.1c02037.

[9] K. Jo, J. Ha, T. Lim, H. Lee, Insulative phase formation and polarization resistance of PrBaCo₂₋ₓCuₓO₅₊δ under thermal stress, Appl. Sci. 12 (2022) 151, https://doi.org/10.3390/app12010151.

[10] A. Cester, A. Rizzo, A. Bazzega, N. Lago, J. Favaro, M. Barbato, N. Wrachien, S. A. Gevorgyan, M. Corazza, F.C. Krebs, Effects of constant voltage and constant current stress in PCBM:P3HT solar cells, Microelectron. Reliab. 55 (2015), https://doi.org/10.1016/j.microrel.2015.06.082.

[11] L. Flannery, J. Ogle, D. Powell, C. Tassone, L. Whittaker-Brooks, Voltage bias stress effects in metal halide perovskites are strongly dependent on morphology and ion migration pathways, J. Mater. Chem. A 8 (2020) 25109–25119, https://doi.org/10.1039/d0ta10371c.

[12] A.C. Teloeken, D.A. Lamb, T.O. Dunlop, S.J.C. Irvine, Effect of bending test on the performance of CdTe solar cells on flexible ultra-thin glass produced by MOCVD, Sol. Energy Mater. Sol. Cells 211 (2020), 110552, https://doi.org/10.1016/j.solmat.2020.110552.

[13] S.K. Laha, P.K. Sadhu, R.S. Dhar, R. Dey, S. Bhattacharya, A. Ganguly, A.K. Naskar, Analysis of mechanical stress and structural deformation on a solar photovoltaic panel through various wind loads, Microsyst. Technol. 27 (2021) 3465–3474, https://doi.org/10.1007/s00542-020-05142-8.

[14] R. Larciprete, A. Agresti, S. Pescetelli, H. Pazniak, A. Liedl, P. Lacovig, D. Lizzit, E. Tosi, S. Lizzit, A. Di Carlo, Mixed cation halide perovskite under environmental and physical stress, Materials 14 (2021) 3954, https://doi.org/10.3390/ma14143954.

[15] M. Mohammadi, S. Gholipour, M. Malekshahi Byranvand, Y. Abdi, N. Taghavinia, M. Saliba, Encapsulation strategies for highly stable perovskite solar cells under severe stress testing: damp heat, freezing, and outdoor illumination conditions, ACS Appl. Mater. Interfaces 13 (2021) 45455–45464, https://doi.org/10.1021/acsami.1c11628.

[16] L. Shi, T.L. Young, J. Kim, Y. Sheng, L. Wang, Y. Chen, Z. Feng, M.J. Keevers, X. Hao, P.J. Verlinden, M.A. Green, A.W.Y. Ho-Baillie, Accelerated lifetime testing of organic-inorganic perovskite solar cells encapsulated by polyisobutylene, ACS Appl. Mater. Interfaces 9 (2017) 25073–25081, https://doi.org/10.1021/acsami.7b07625.

[17] S. Spataru, P. Hacke, D. Sera, In-situ measurement of power loss for crystalline silicon modules undergoing thermal cycling and mechanical loading stress testing, Energies 14 (2021) 72, https://doi.org/10.3390/en14010072.

[18] A. Di Carlo, F. Matteocci, S. Razza, M. Mincuzzi, F. Di Giacomo, S. Casaluci, D. Gentilini, T.M. Brown, A. Reale, F. Brunetti, A. D'Epifanio, S. Licoccia, Mesoscopic perovskite solar cells and modules, in: 14th IEEE Int. Conf. Nanotechnol., IEEE, 2014, pp. 70–74, https://doi.org/10.1109/NANO.2014.6968015.

[19] G. Tang, T. Wang, J. Cao, Z. Zhao, J. Song, P. Liu, H. Cheng, F. Zheng, J. Zhao, F. Yan, Highly stable and efficient perovskite solar cells passivated by a functional amorphous layer, J. Mater. Chem. A 9 (2021) 21708–21715, https://doi.org/10.1039/d1ta07505e.

[20] B. Li, M. Lin, C. Kan, P. Hang, Y. Yao, Z. Hu, Y. Wang, Y. Zhang, W. Zhong, D. Yang, X. Yu, Revealing the correlation of light soaking effect with ion migration in perovskite solar cells, Sol. RRL 6 (2022), 2200050, https://doi.org/10.1002/solr.202200050.

[21] L. Lin, L. Yang, G. Du, X. Li, Y.N. Li, J. Deng, K. Wei, J. Zhang, Light soaking effects in perovskite solar cells: mechanism, impacts, and elimination, ACS Appl. Energy Mater. (2022), https://doi.org/10.1021/acsaem.2c04120.

[22] A. Kumar, U. Bansode, S. Ogale, A. Rahman, Understanding the thermal degradation mechanism of perovskite solar cells via dielectric and noise measurements, Nanotechnology 31 (2020), 365403, https://doi.org/10.1088/1361-6528/ab97d4.

[23] M. Thambidurai, M.I. Omer, F. Shini, H.A. Dewi, N.F. Jamaludin, T.M. Koh, X. Tang, N. Mathews, C. Dang, Enhanced thermal stability of planar perovskite solar cells through triphenylphosphine interface passivation, ChemSusChem 15 (2022), e202102189, https://doi.org/10.1002/cssc.202102189.

[24] S. Bae, S. Kim, S.W. Lee, K.J. Cho, S. Park, S. Lee, Y. Kang, H.S. Lee, D. Kim, Electric-field-induced degradation of methylammonium lead iodide perovskite solar cells, J. Phys. Chem. Lett. 7 (2016) 3091–3096, https://doi.org/10.1021/acs.jpclett.6b01176.

[25] M.V. Khenkin, E.A. Katz, A. Abate, G. Bardizza, J.J. Berry, C. Brabec, F. Brunetti, V. Bulović, Q. Burlingame, A. Di Carlo, R. Cheacharoen, Y.B. Cheng, A. Colsmann, S. Cros, K. Domanski, M. Dusza, C.J. Fell, S.R. Forrest, Y. Galagan, D. Di Girolamo, M. Grätzel, A. Hagfeldt, E. von Hauff, H. Hoppe, J. Kettle, H. Köbler, M.S. Leite, S. Frank Liu, Y.L. Loo, J.M. Luther, C.Q. Ma, M. Madsen, M. Manceau, M. Matheron, M. McGehee, R. Meitzner, M.K. Nazeeruddin, A.F. Nogueira, Ç. Odabaşı, A. Osherov, N.G. Park, M.O. Reese, F. De Rossi, M. Saliba, U. S. Schubert, H.J. Snaith, S.D. Stranks, W. Tress, P.A. Troshin, V. Turkovic, S. Veenstra, I. Visoly-Fisher, A. Walsh, T. Watson, H. Xie, R. Yıldırım, S. M. Zakeeruddin, K. Zhu, M. Lira-Cantu, Consensus statement for stability assessment and reporting for perovskite photovoltaics based on ISOS procedures, Nat. Energy 51 (5) (2020) 35–49, https://doi.org/10.1038/s41560-019-0529-5, 2020.

[26] F. Di Giacomo, L.A. Castriotta, F.U. Kosasih, D. Di Girolamo, C. Ducati, A. Di Carlo, Upscaling inverted perovskite solar cells: optimization of laser scribing for highly efficient mini-modules, Micromachines 11 (2020) 1–13, https://doi.org/10.3390/mi11121127.

[27] S.H. Reddy, F. Di Giacomo, F. Matteocci, L.A. Castriotta, A. Di Carlo, Holistic approach toward a damage-less sputtered indium tin oxide barrier layer for high-

stability inverted perovskite solar cells and modules, ACS Appl. Mater. Interfaces 14 (2022) 51438–51448, https://doi.org/10.1021/acsami.2c10251.

[28] IEC 60904–7:2019; Photovoltaic Devices—Part 7: Computation of the Spectral Mismatch Correction for Measurements of Photovoltaic Devices, BSI Standards Limited, London, UK, 2019. ISBN 978-0-580-97364-2.

[29] A. Rizzo, A. Cester, L. Torto, M. Barbato, N. Wrachien, N. Lago, M. Corazza, F. C. Krebs, S.A. Gevorgyan, Effects of current stress and thermal storage on polymeric heterojunction P3HT:PCBM solar cell, in: IEEE Int. Reliab. Phys. Symp. Proc., 2016, pp. 3C21–3C26, https://doi.org/10.1109/IRPS.2016.7574523.

[30] R. Sokel, R.C. Hughes, Numerical analysis of transient photoconductivity in insulators, J. Appl. Phys. 53 (1998) 7414, https://doi.org/10.1063/1.330111.

[31] J. Liu, G. Wang, K. Luo, X. He, Q. Ye, C. Liao, J. Mei, Understanding the role of the electron-transport layer in highly efficient planar perovskite solar cells, ChemPhysChem 18 (2017) 617–625, https://doi.org/10.1002/cphc.201601245.

[32] C. Chen, S. Zhang, S. Wu, W. Zhang, H. Zhu, Z. Xiong, Y. Zhang, W. Chen, Effect of BCP buffer layer on eliminating charge accumulation for high performance of inverted perovskite solar cells, RSC Adv. 7 (2017) 35819–35826, https://doi.org/10.1039/c7ra06365b.

[33] D. Di Girolamo, N. Phung, F.U. Kosasih, F. Di Giacomo, F. Matteocci, J.A. Smith, M. A. Flatken, H. Köbler, S.H. Turren Cruz, A. Mattoni, L. Cinà, B. Rech, A. Latini,

G. Divitini, C. Ducati, A. Di Carlo, D. Dini, A. Abate, Ion migration-induced amorphization and phase segregation as a degradation mechanism in planar perovskite solar cells, Adv. Energy Mater. 10 (2020), 2000310, https://doi.org/10.1002/aenm.202000310.

[34] J.W. McPherson, Reliability Physics and Engineering: Time-To-Failure Modeling, third ed., Springer International Publishing, Cham, 2019 https://doi.org/10.1007/978-3-319-93683-3.

[35] J. Lim, M. Kim, H.H. Park, H. Jung, S. Lim, X. Hao, E. Choi, S. Park, M. Lee, Z. Liu, M.A. Green, J. Seo, J. Park, J.S. Yun, Kinetics of light-induced degradation in semi-transparent perovskite solar cells, Sol. Energy Mater. Sol. Cells 219 (2021), 110776, https://doi.org/10.1016/j.solmat.2020.110776.

[36] D.B. Khadka, Y. Shirai, M. Yanagida, K. Uto, K. Miyano, Analysis of degradation kinetics of halide perovskite solar cells induced by light and heat stress, Sol. Energy Mater. Sol. Cells 246 (2022), 111899, https://doi.org/10.1016/j.solmat.2022.111899.

[37] N. Lago, A. Polo, S.H. Reddy, A. Di Carlo, A. Cester, Intrinsic instability of perovskite solar cells: the role of a hole-blocking layer, Crystals 13 (2023) 185, https://doi.org/10.3390/cryst13020185.